Rhombohedral distortion-driven ferroelectric order and exchange bias effect in geometrically frustrated ZnFe2O4

1 author:

Jayjit Kumar Dey
Indian Association for the Cultivation of Science

6 PUBLICATIONS   **36** CITATIONS

SEE PROFILE

Rhombohedral distortion-driven ferroelectric order and exchange bias effect in geometrically frustrated ZnFe₂O₄

J. K. Dey,[1] A. Chatterjee,[1] A.-C. Dippel,[2] O. Gutowski,[2] M. v. Zimmermann,[2] S. Majumdar,[1] and S. Giri[1,*]

[1]*School of Physical Sciences, Indian Association for the Cultivation of Science, Jadavpur, Kolkata 700032, India*
[2]*Deutsches Elektronen-Synchrotron DESY, Notkestrasse 85, 22607 Hamburg, Germany*

The rhombohedral distortion-driven occurrence of the spontaneous electric polarization at a reasonably high temperature (T) and an exchange bias (EB) effect below the antiferromagnetic (AFM) Néel temperature (T_N) are revealed in ZnFe₂O₄. We observe the magnetic memory effect, suggesting a cooperative glassy magnetic state below T_N. The phase separation between the long-range AFM and the glassy magnetic component leads to the EB effect below T_N. The synchrotron diffraction studies confirm a structural transition to a polar $R3m$ structure from the cubic spinel structure, involving a strong rhombohedral distortion. This distortion correlates with the occurrence of the spontaneous electric polarization (P) below $\sim$110 K (T_{FE1}), which is accompanied by a short-range order (SRO). The P-value enhances further due to an additional rhombohedral distortion below T_N. A considerable magnetoelectric (ME) coupling is detected below T_{FE1}. The increase of P is $\sim$7.2% for 5 T at the liquid nitrogen temperature. There has been a fundamental interest among the community in the unique result of the occurrence of ferroelectric (FE) order coexisting with SRO and having a significant ME coupling, which is accompanied by a strong rhombohedral structural distortion analogous to that observed in BiFeO₃.

I. INTRODUCTION

AB_2X_4-type compounds continue to inspire interest in magnetism due to the tuning of the A and B atoms, which are crystallized in the spinel structure. Here, X represents either the oxygen or the chalcogenides. For example, the solely A-site magnetic atom in the spinel structure gives rise to exotic effects such as spin dimerization [1], spin liquid ground states [2–4], and suppressed antiferromagnetic order [5], which are often regulated by either orbital ordering or geometric magnetic frustrations, or both. Transition elements in both the A- and B-sites reduce the magnetic frustration, but this produces interesting consequences such as structural instabilities [6–8], intricate magnetic structures [9,10], ferroelectricity [11–14], etc. The solely B-site magnetic atom in AB_2X_4 is found to have potential for the pyrochlore structure, producing strong geometric magnetic frustration [15,16]. The geometrically frustrated pyrochlore structure becomes the center of attraction when it reveals interesting fallout, specifically various spin ice states [17–19], charge ordering [20,21], and intricate magnetic structures [22,23].

The spinel Zn-ferrite ZnFe₂O₄ (ZFO) attracts special attention due to the B-site magnetic frustration, which is attributed to the pyrochlore structure [24]. An example of a pyrochlore structure formed solely by Fe atoms in the $Fd\bar{3}m$ structure is depicted in Fig. 1(a). The structure is composed of corner-sharing tetrahedra, where four corners of a tetrahedron are occupied by the Fe atom. In the case of antiferromagnetic (AFM) exchange interaction, a tetrahedral unit is highly frustrated, as depicted by the question marks in Fig. 1(b).

Long-range AFM order at T_N has been reported, suggesting T_N is in the range of 10.5–13 K by means of the neutron, μ-SR, and Mössbauer studies [25,26]. The T_N at 13 K was proposed with a high paramagnetic Curie-Weiss temperature, $\Theta = 120$ K, which provided a high value of the Θ/T_N ratio, pointing to strong magnetic frustration [26]. The density functional theory further interpreted the nature of the AFM order [27,28]. Revisiting the Mössbauer studies, it was proposed that the disorder, either introduced by the external pressure or the internal pressure attributed to the chemical disorder, was found to be crucial for tuning the magnetism of ZFO [29–32]. The external pressure effect demonstrated an irreversible change in the unit-cell volume, correlating with a change in the spin state [31]. The chemical disorder-driven spin-glass and/or cluster-glass state was proposed [32], which was also interpreted from *ab initio* calculations [33]. The magnetic diffuse scattering results proposed a spin liquid state, analogous to the three-dimensional (3D) quantum spin liquid system, Y(Sc)Mn₂, which was attributed to the strong magnetic frustration [34,35]. For the dominant short-range order (SRO), preferably, the existence of a ferromagnetic (FM) cluster has been proposed in nanoscale ZFO from neutron polarization studies [36]. In fact, a dominant SRO has been proposed from the neutron diffraction studies of a ZFO crystal, which was suggested to occur around 10 times ($\sim$105 K) for T_N at 10.5 K, and also proposed to exist a SRO state even below T_N [25]. Up to now, a lot of attention has been paid to the magnetic ground state below T_N using different microscopic experimental tools, although the physical origin of the SRO, observed at much higher than T_N, remains unaddressed.

In the article, we report significant magnetoelastic coupling close to the proposed emergence of SRO for ZFO. We observe a structural transition to a polar structure with a $R3m$
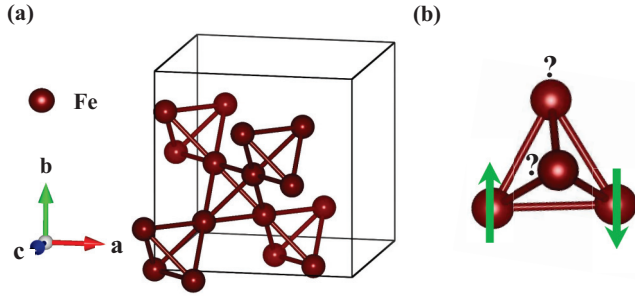
*sspsg2@iacs.res.in

FIG. 1. (a) A part of the pyrochlore structure formed by the Fe atoms crystallized in $Fd\bar{3}m$ structure within the unit cell. (b) Antiferromagnetically coupled tetrahedron unit, with examples of the magnetic frustrations denoted by the "?" marks.

FIG. 2. (a) Zn $2p$ and (b) Fe $2p$ core level XPS of ZFO. (c) ^{57}Fe Mössbauer spectrum recorded in the transmission mode at 300 K. The fits in (a), (b), and (c) are shown by the solid curves. (d) SEM image highlighting the particles.

space group from the cubic $Fd\bar{3}m$ structure around $\sim$110 K. Intriguingly, this structural transition is associated with a ferroelectric (FE) order with the ordering at $T_{FE1} = 110$ K, which is followed by an evident signature of magnetoelectric (ME) coupling at T_N. The value of electric polarization (P) is considerable as $\sim$125 μC/m^2 at liquid nitrogen temperature for a 500 kV/m poling field. The value of P increases with the application of a magnetic field (B), pointing to ME coupling. The P increases up to $\sim$7.2% for $B = 5$ T at liquid nitrogen temperature. The dc magnetization results show the magnetic memory effect in the thermal variation as well as relaxation dynamics below T_N, pointing to a signature of a cooperative glassy magnetic behavior. The glassy magnetic component coexisting with the AFM ordered state leads to the emergence of an exchange bias (EB) effect due to the field-cooling below T_N. The value of the EB field is reasonable: $\sim$6.7 mT at 2 K for a cooling field of 1 T. Current investigation has unfolded the important issues close to T_N and T_{FE1}. At T_N, a strong rhombohedral distortion is proposed, which is accompanied by an increase in the FE polarization and a magnetic phase separation, giving rise to the EB effect. The structural transition to a polar $R3m$ structure at T_{FE1}, which involves a strong rhombohedral distortion, is very similar to the observed ferroelectricity driven by the rhombohedral distortion in the $R3m$ structure for BiFeO$_3$ [37,38].

II. EXPERIMENTAL RESULTS

Polycrystalline ZnFe$_2$O$_4$ is prepared using a standard solid-state reaction technique [25]. The chemical composition is checked by x-ray diffraction at room temperature recorded in a PANalytical x-ray diffractometer (model: X' Pert PRO) using Cu $K\alpha$ radiation. The single-phase chemical composition is further confirmed by the synchrotron diffraction recorded with a wavelength of 0.1422 Å (87.1 keV) at the P07 beamline of PETRA III, Hamburg, Germany. The synchrotron diffraction data are analyzed using Rietveld refinement with commercially available MAUD software. The polycrystalline sample, pressed into a pellet, is used for the dielectric measurements, using an E4980A LCR meter (Agilent Technologies, USA) equipped with a commercial PPMS Evercool-II system of Quantum Design. The pyroelectric current (I_p) is recorded in an electrometer (Keithley, model 6517B) at a constant temperature sweep rate. In all

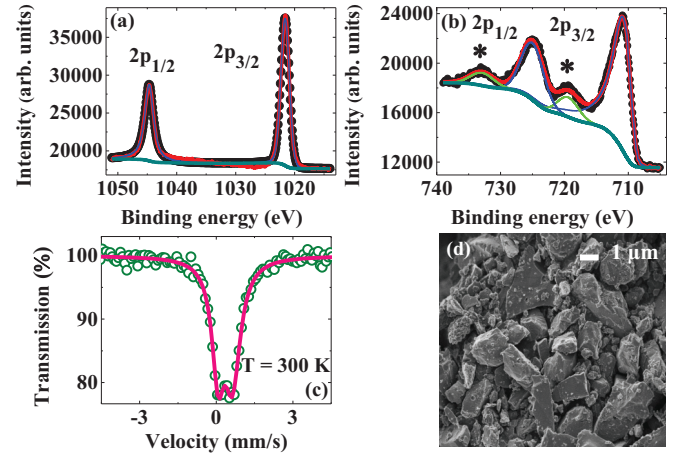the measurements, the electrical contacts are fabricated using air-drying silver paint. The poling electric fields are applied during cooling processes, and the values of I_p are measured in the warming mode in zero electric field. Before the measurement of I_p, the electrical connections are short-circuited and left to wait for a sufficiently long time. Magnetization is measured in a commercial magnetometer of Quantum Design (MPMS, Evercool). Scanning electron microscopy (SEM) is performed using a JEOL JSM-6010LA. X-ray photoemission spectroscopy (XPS) is recorded with a spectrometer of Omicron Nanotechnology. The Mössbauer spectrum is recorded in a transmission geometry using a ^{57}Co source fixed in a Rh matrix, where a Wissel velocity drive unit is used in a constant acceleration mode. The Mössbauer parameters are estimated with respect to the α-Fe.

III. EXPERIMENTAL RESULTS AND DISCUSSIONS

A. Chemical and physical characterization

The Zn $2p$ and Fe $2p$ core level XPS of ZFO are summarized in Figs. 2(a) and 2(b). In Fig. 2(a), the two peaks observed at 1021.6 and 1044.7 eV correspond to the $2p_{3/2}$ and $2p_{1/2}$ peaks of Zn, respectively. Figure 2(b) depicts the spectrum with the peaks at 725 and 710.9 eV for Fe $2p_{1/2}$ and $2p_{3/2}$, respectively. The satisfactory fits are shown by the solid curves on the experimental data in both figures. The results indicate the Zn^{2+} and Fe^{3+} states in ZFO, as reported earlier [39–41]. We note that the ratio of the area under the curve of the Zn- and Fe-spectrum is close to 1:2, which is reasonable for the composition of ZnFe$_2$O$_4$. To further confirm the oxidation state of Fe, the Mössbauer spectrum is recorded at 300 K, as depicted in Fig. 2(c). The paramagnetic state, as indicated by the doublet spectrum, is realized with an isomer shift (IS) of 0.36 mm/s and a quadrupole splitting (QS) of 0.45 mm/s. The value of the IS is consistent with that observed for the high-spin Fe^{3+} state [29,30]. Figure 2(d) illustrates the SEM image. The average grain size is obtained using the mean lineal intercept technique, $D_{\text{average}} = 1.56L/MN$, where
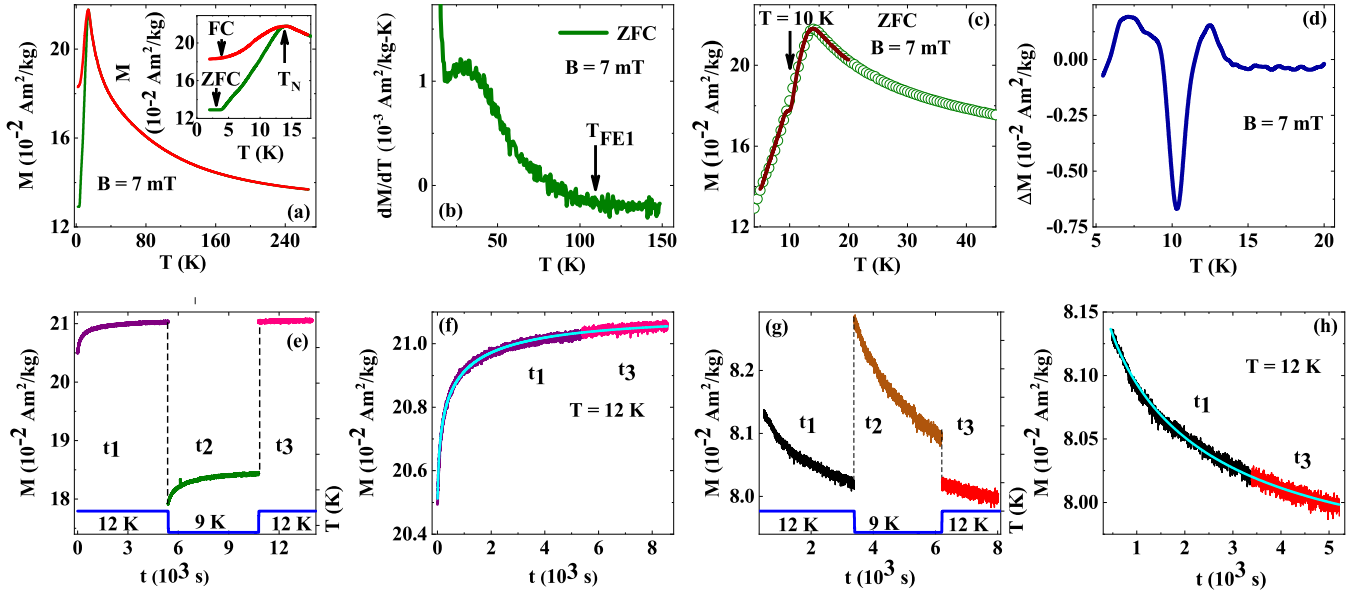
FIG. 3. (a) The T variations of ZFC-FC magnetization curves recorded at 7 mT. The arrow in the inset highlights T_N, below which ZFC and FC magnetization curves deviate from each other. (b) The dM/dT with T recorded in ZFC mode, highlighting T_{FE1}. (c) The T variation of the ZFC curve recorded at 7 mT, defined as a reference curve and the memory curve, as indicated by the solid curve. The arrow indicates the aging temperature at 10 K. (d) Difference between these curves shown by ΔM plotted with T, highlighting a sharp "dip" close to 10 K. (e) The t dependence of M at 12 K, 9 K, and again at 12 K for $t1$, $t2$, and $t3$, respectively, with 7 mT after cooling in ZFC mode. (f) The t dependence of M at 12 K for $t1 + t3$ recorded at 7 mT, following a single stretched exponential function. (g) The t dependence of M at 12 K, 9 K, and again at 12 K for $t1$, $t2$, and $t3$, respectively in zero-field after cooling in FC mode with a field of 7 mT. (f) t dependence of M at 12 K for $t1 + t3$ in zero-field, following a single stretched exponential function. The T vs t plots for the experiments in ZFC and FC modes are shown at the bottom of panels (e) and (g), respectively.

$D_{average}$ is the average grain size, L is the total length of test line used, N is the number of intercepts, and M is the magnification of the SEM image. Here, the proportionality constant, 1.56, is essentially a correction factor, which was derived by Mendelson [42]. The value of $D_{average}$ is 2.6 μm with a standard deviation of 0.33.

B. Short-range order above T_N

Thermal variations of magnetization (M) are recorded in the zero-field-cooled (ZFC) and field-cooled (FC) protocols, which are shown in Fig. 3(a) for $B = 7$ mT. A sharp peak is observed in both the ZFC and FC curves, below which they deviate from each other at 13.5 K (T_N), as depicted in the inset of the figure. The result is consistent with the reported results [26]. Figure 3(b) depicts a derivative plot of M (dM/dT) recorded in the ZFC mode with temperature (T). The curve indicates that with decreasing temperature it starts to increase slowly below T_{FE1}, as indicated by an arrow. Here, T_{FE1} denotes the FE Curie temperature, which is described elsewhere in the text. The $dM/dT (T)$ curve is consistent with the previous report, indicating the occurrence of SRO [25]. Here, we note that the SRO starts to appear significantly close to T_{FE1}.

C. Magnetic memory effect below T_N

To investigate the magnetic memory effect, the sample is cooled from 300 K down to 10 K ($< T_N$) in zero field and left to wait for 3600 s (t_w), which is followed by further cooling down to 2 K. Next, the magnetization is recorded in the warming mode with 7 mT for a temperature sweep rate of 1 K/min. The magnetization curve is recorded up to 20 K, which is depicted by a continuous curve with T in Fig. 3(c). We notice an apparent signature of anomaly at 10 K, which is further compared with the reference curve, as shown by the open symbols in the figure. Here, the reference curve is the same ZFC curve as shown in Fig. 3(a). The difference between these two, defined as ΔM, is depicted in Fig. 3(d). The ΔM versus T plot clearly shows a "dip" at 10 K, revealing the memory effect. The result is consistent with that observed for spin-glass systems [43]. During the aging process at 10 K, the system is allowed to relax and it rearranges the spin configuration toward the equilibrium. This equilibrium state is frozen with a further cooling process, which can be retrieved during measurement on reheating the system. The magnetic memory effect observed in the ZFC mode suggests the cooperative glassy dynamics, as commonly observed for the spin glasses [43].

To verify the memory effect further, experiments on the relaxation dynamics are carried out using the experimental protocols proposed in the literature [44]. All the experimental results are summarized in Figs. 3(e)–3(h). At first, the relaxation of M is recorded for a time period of $t1$ at 12 K (below T_N) with 7 mT, after cooling the sample in zero-field from 300 K. At the end of $t1$, the sample temperature is lowered to 9 K and the relaxation is recorded for $t2$. Finally, the sample temperature is heated back to 12 K and the relaxation is recorded for $t3$, as shown in Fig. 3(e). The changes of temperature with time are depicted at the bottom of the figure.

As displayed in Fig. 3(f), the relaxation processes during $t1 + t3$ at 12 K follow a single stretched exponential function [45,46]. Similar results are observed for the relaxation dynamics measured in zero field at 12 K after cooling the sample in FC mode with $B = 7$ mT from 300 K, as shown in Fig. 3(g). Similar to the experiment in the ZFC mode, the changes in temperature with time during the experiment are depicted at the bottom of the figure. Figure 3(h) depicts the relaxation process in zero field for $t1 + t3$ at 12 K, following a single stretched exponential function. The results demonstrate that the relaxation process after the temporary cooling for $T - \Delta T$ retrieves the previous history, pointing to the manifestations of the memory effect in the relaxation dynamics. Thus, the memory effects in both the thermal variation as well as relaxation dynamics suggest a glassy magnetic state. The glassy magnetic state, coexisting with the long-range AFM order below T_N, is analogous to that observed for $ZnCr_2O_4$ [47]. A considerable EB effect was observed for $ZnCr_2O_4$, which was attributed to the coexisting magnetic phases below T_N [47].

D. Exchange bias effect below T_N

Figure 4(a) depicts the magnetic hysteresis loop recorded at 2 K, having a considerable coercive field (H_C). As depicted in the inset of the figure, the loop closes around ~1.4 T, above which almost a linear magnetization curve is observed, as noted for the AFM ground state. The opening of the loop in the low-field region for an AFM ground state indicates an additional magnetic phase coexisting with the AFM phase below T_N, which has also been reported earlier from the combined neutron, μ-SR, and Mössbauer studies [25]. Here, the glassy magnetic component, as indicated by the memory effect, coexisting with the AFM component, may lead to the occurrence of the EB effect even in a chemically single phase compound [48]. To test it, initially, we cool the sample down to 2 K with the cooling field of ± 1 T and the hysteresis loop is measured in between ± 5 T (H_{max}), as depicted in Fig. 4(a). The inset of the figure highlights that the loop closes around ~1.4 T, which is less than 1/3 of H_{max}. A negative shift for the positive cooling field and a positive shift for the negative cooling field are depicted in Figs. 4(b) and 4(c), respectively. This manifestation is typical for the EB effect [49–53]. We further note that the field-cooling from the temperatures above T_{FE1} or T_N does not significantly influence the EB effect. From the shift of the hysteresis loop in the field axis, the EB field is defined as $H_E = -(H_1 + H_2)/2$ and $H_C = (H_2 - H_1)/2$ for a positive cooling field, where H_1 and H_2 are the left and right coercive fields, respectively.

The values of H_E and H_C at 2 K for a cooling field of 1 T are depicted in Figs. 4(d) and 4(e), respectively. Initially, the EB field increases with increasing cooling field up to 1 T, which is associated with the increase in the coercive field. This observation is an indication of the appearance of a magnetic phase with the considerably increased anisotropy driven by the cooling field. Thus the field-cooling process gives rise to the emergence of a new layer composed of the pinned spins at the interface between the AFM and the glassy magnetic phases. The possible occurrence of a pinned layer at the interface between the AFM and glassy magnetic layer is illustrated in the inset of Fig. 4(d). The pinned layer, carrying
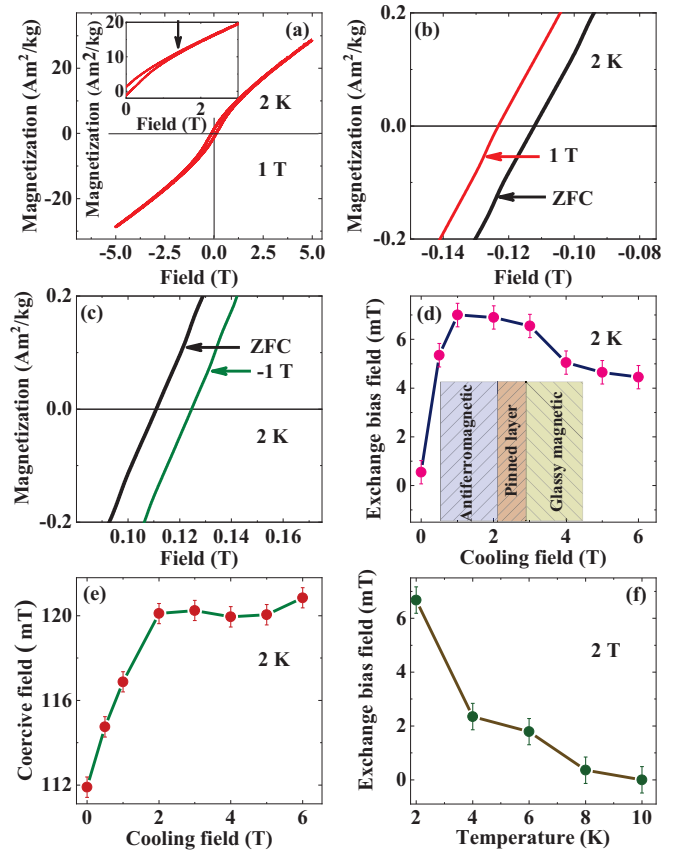

FIG. 4. (a) Hysteresis loop recorded up to maximum field of ± 5 T at 2 K for a cooling field of 1 T. The inset highlights that the loop closes around 1.4 T, as indicated by an arrow. (b) Negative and (c) positive shifts are shown for a cooling field of ± 1 T. Cooling field dependence of (d) EB field and (e) coercive field at 2 K. Temperature variation of (f) EB field for a cooling field of 2 T. The inset of (d) illustrates a representative illustration of the occurrence of a pinned layer at the interface between AFM and glassy magnetic phases.

the unidirectional anisotropy, causes a systematic shift of the hysteresis loop driven by the cooling field and leads to the EB effect. This unidirectional anisotropy strongly depends on the individual anisotropy of the magnetic phases coupled with the pinned layer. We note that with a further increase in the cooling field above 1 T, the EB field shows a decreasing trend, which is often observed for the exchange bias effect, involving the glassy magnetic component [54–57]. When the cooling field is high, the frozen spins, belonging to the glassy magnetic component, are almost fully aligned and vary a little along the field with a further increase in the higher cooling field. As a result of it, the magnetic coupling between the strong cooling field and the glassy magnetic moment increases, tending to polarize them along the field direction, where the magnetic coupling dominates over the EB coupling. This may lead to a decrease in the EB field at the higher cooling field. As depicted in Fig. 4(f), the EB field decreases with decreasing temperature and nearly vanishes close to T_N. The result indicates that the AFM state below T_N leads to a crucial role for the EB effect.
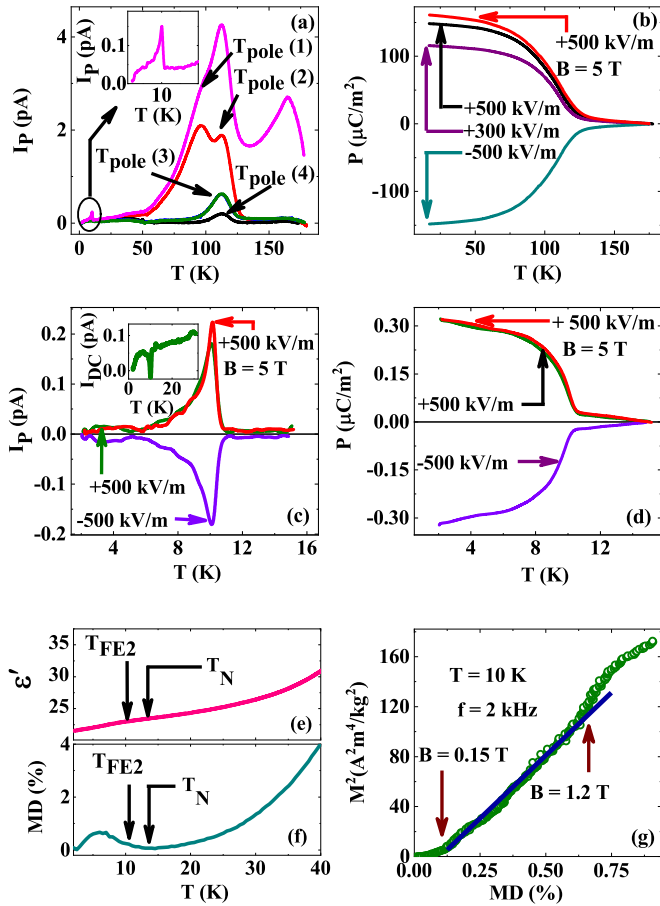
FIG. 5. The T variations of (a) I_p recorded with a constant T-sweep rate of 5 K/min at different poling temperatures (T_{pole}), as described in the text and for a poling field (E) of 500 kV/m; (b) P for $E = +300, \pm 500$ kV/m, and 500 kV/m with a magnetic field of 5 T; (c) I_p for $E = \pm 500$ kV/m and the same with a magnetic field of 5 T for T_{pole} at 15 K; and (d) P, as calculated from the data given in (c). The inset of (a) highlights another low-T peak and (c) shows the dc bias current (I_{DC}) with T with a "dip" at ~ 10.5 K. The T variations of (e) ϵ' at $f = 2$ kHz and (f) MD(%), showing T_{FE2} and T_N by the arrows. Plot of (g) M^2 with MD(%) at 10 K for $f = 2$ kHz.

E. Ferroelectric order above T_N

Figure 5(a) shows a temperature variation of the pyroelectric current (I_p) recorded with the poling electric field of 500 kV/m and a thermal sweep rate of 5 K/min in the different poling conditions. To confirm the peak in $I_p(T)$, appearing due to a genuine occurrence of the polar order, the values of $I_p(T)$ are recorded for the different poling temperatures. In the figure, T_{pole} (1), T_{pole} (2), T_{pole} (3), and T_{pole} (4) represent the poling temperatures at 150, 95, 20, and 8 K, respectively. In all the cases, a peak at 110 K is always observed, pointing to a genuine occurrence of the peak [7,58,59], which is shown in the figure. For T_{pole} (1) another high-temperature peak is observed, which disappears with T_{pole} close to or below the polar order. The high-T peak appears due to the extrinsic thermally stimulated depolarization currents (TSDC) [7,58–60]. For the poling at 95 K, an additional peak close to 95 K appears below the peak at 110 K. The peak around 95 K disappears for poling at 150, 20, and 8 K, although the peak at 110 K is

always evident, which is described as T_{FE1}. After subtracting the TSDC component for T_{pole} at 150 K, the $I_p(T)$, integrated with time, provides the thermal variation of P. The $P(T)$ curves are depicted in Fig. 5(b) for different poling fields. The $P(T)$ curve reverses almost symmetrically due to a change of sign of the poling field, pointing to the FE nature of the polar order. The value of P at 15 K is ~ 148 $\mu C/m^2$ for a poling field of 500 kV/m. With the application of a magnetic field, the P-value increases, pointing to a significant ME. The changes of P due to a 5 T magnetic field are 7.2 (%) and 8.6 (%) at the liquid nitrogen temperature and 17 K, respectively.

We note that another peak is observed in $I_p(T)$ close to T_N for T_{pole} (1), as highlighted in the inset of Fig. 5(a). To focus on this low-T peak, the poling is further done at 15 K with a temperature sweep rate of 5 K/min for a poling field of ± 500 kV/m. As depicted in Fig. 5(c), the $I_p(T)$ exhibits a sharp peak at 10.5 K, which reverses due to a change in sign of the poling field, pointing to the FE nature of the additional polar order below T_N. The inset of the figure shows a sharp "dip" in the bias current (I_{DC}), which is recorded in the heating cycle with a thermal sweep rate of 5 K/min and a bias electric field of 500 kV/m. Thus the sharp peak in $I_p(T)$ is genuinely observed at 10.5 K (T_{FE2}). Integration of $I_p(T)$ with time provides $P(T)$, which is shown in Fig. 5(d). With the application of a 5 T magnetic field, the $P(T)$ does not change convincingly, as also indicated in Fig. 5(d).

F. Dielectric and magnetodielectric effect

Dielectric permittivity (ϵ) is recorded with T at a fixed frequency (f), for example at $f = 2$ kHz for a magnetic field (B) of 0 and 5 T. Thermal variation of the real (ϵ') component of ϵ is shown in Fig. 5(e). We note that the value of ϵ' is not reliable above ~ 40 K, which is attributed to the low resistivity. To test the reliable value of ϵ' below ~ 40 K, we calculate the value of P/E, which is found close to the value of ϵ'. The value of P/E is ~ 33 for $E = 500$ kV/m, which is quite reasonable for $\epsilon' \approx 24$ at 16 K. This discrepancy may be attributed to the nonlinear behavior of the P-E curve close to $E = 500$ kV/m. The percentage of magnetodielectric (MD) response, defined as $[\epsilon'(B)/\epsilon'(B = 0) - 1] \times 100$, is depicted with T for $B = 5$ T in Fig. 5(f). T_N and T_{FE2} are highlighted by the arrows. A minimum in MD(T) is noted around T_N. Below T_{FE2}, the MD(T) shows a maximum around 7 K.

The MD consequences are correlated to the ME coupling, which have been phenomenologically expressed using the Ginzburg-Landau theory through the ME coupling term $\gamma P^2 M^2$ in the thermodynamic potential (Φ), which is defined as

$$\Phi = \Phi_0 + \alpha P^2 + \frac{\beta}{2}P^4 - PE + \alpha' M^2 + \frac{\beta'}{2}M^4 - MB$$
$$+ \gamma P^2 M^2. \tag{1}$$

Here, α, β, α', β', and γ are the constants and functions of temperature. In the magnetically ordered state, the influence of magnetic order on the MD response is followed by a linear response of the M^2 versus MD(%) curve. Here, the M^2 with MD(%) plot at 10 K is shown in Fig. 5(g). We note that the linearity of the curve holds satisfactorily for $0.15 \leqslant B \leqslant 1.2$ T, as indicated by the arrows. The linearity
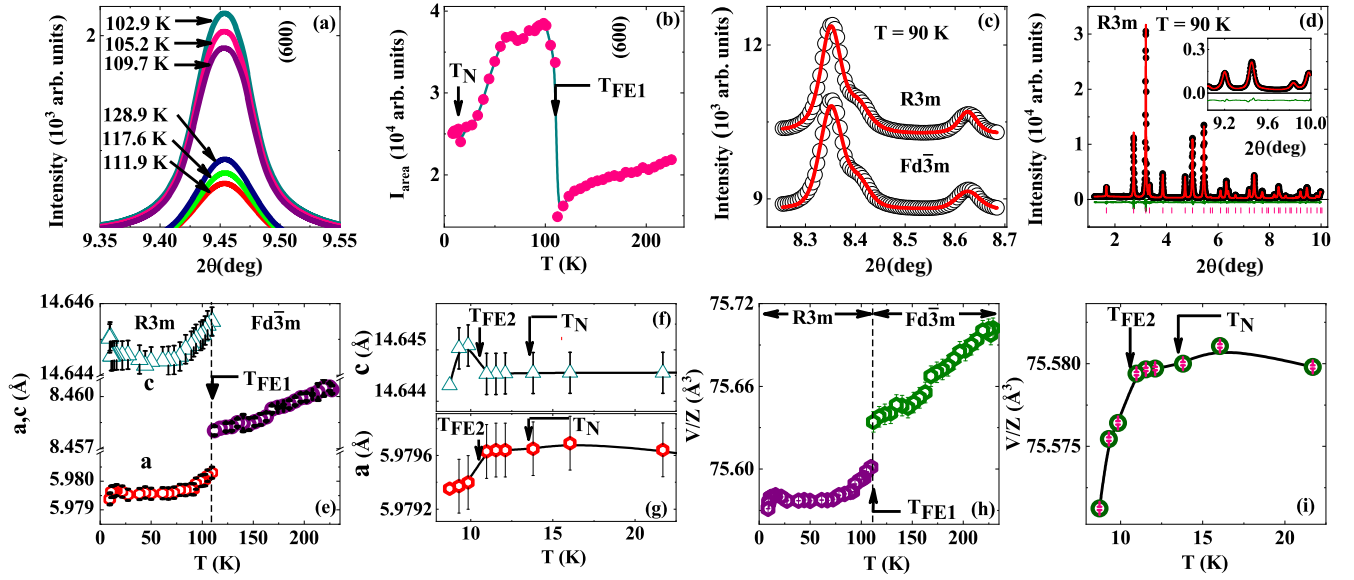
FIG. 6. (a) High-2θ peaks shown at different T around T_{FE1} at 110 K. (b) Integrated intensity (I_{area}) of (600) peak with T, showing arrows at T_{FE1} and T_N. Comparison of (c) the refinements (red solid curve) of the selected 2θ peaks at 90 K using $Fd\bar{3}m$ and $R3m$ space groups. Rietveld refinement of the (d) diffraction pattern at 90 K using $R3m$ structure. The inset amplifies the result on the quality of refinement in a selected high-2θ region. The T variations of (e) refined lattice constants, a and c in range of 8.7–250 K, (f) c, and (g) a at low-T with $R3m$ structure, highlighting T_{FE2} and T_N by the arrows, (h) V in the entire T range, and (i) V at low-T, showing T_{FE2} and T_N.

of the plot indicates that the ME coupling term $\gamma P^2 M^2$ of the Ginzburg-Landau theory is significant for ZFO, as reported earlier for the different multiferroics [14,45,47,61–63].

G. Structural correlation to the ferroelectric order

The structural properties are investigated using the synchrotron diffraction studies over a wide temperature range of 8–250 K and at 300 K. The ZFO crystallizes in the normal spinel structure with the cubic $Fd\bar{3}m$ (No. 227, $Z = 8$) space group at 300 K. At 300 K, the diffraction pattern is satisfactorily refined (not shown here) with the lattice constant, $a = 8.4658(3)$ Å, considering Zn (x, x, x) with $x = 0.3750(0)$, Fe $(0, 0, 0)$, and O (x, x, x) with $x = 0.2412(9)$. The reliability parameters, $R_w(\%) \sim 6.60$, $R_{exp}(\%) \sim 3.39$, and $\chi^2(\%) \sim 1.94$, are found to be reasonable. Figure 6(a) exhibits a peak in a selected high-2θ region, highlighting the T-region close to T_{FE1} in the range of 102.9–128.9 K. Here, the peaks at 109.7 and 111.9 K are the closest to T_{FE1}. From the high temperature, the intensities of the peaks decrease systematically up to 111.9 K, below which they suddenly increase at 109.7 K. The integrated intensity (I_{area}), as estimated by the area under the (600) peak, is depicted with T in Fig. 6(b). I_{area} decreases systematically with decreasing T up to 111.9 K, below which a steplike sharp increase of I_{area} is observed, which is followed by a further increase up to ~100 K. Below 100 K, the I_{area} decreases until ~50 K, below which it shows a steep fall down to ~25 K. A slow decrease in I_{area} is observed below ~25 K.

This intensity change around T_{FE1} is remarkably high as ~ 73%, which is much larger than the results observed for the multiferroics, involving the steplike isostructural changes [13,14] and the structural transitions to the lower symmetries [7,8,45,64]. We note that the refinement is not satisfactory below T_{FE1} with the $Fd\bar{3}m$ structure. The examples of the

refinement of the selected 2θ peaks at 90 K with the $Fd\bar{3}m$ structure are shown in Fig. 6(c) by the continuous curves. We use the ISODISTORT [65] software to find out the possible subgroup structures at the proposed structural transition close to T_{FE1}. We note that $F\bar{4}3m$ (no. 216), $R\bar{3}m$ (no. 166), and $R3m$ (no. 160) are the possible structures with high symmetries. The refinements are performed using all the space groups, which provide the values of the reliability parameters as $R_w(\%) \sim 7.07$, 6.86, 7.33, and 5.96; $R_{exp}(\%) \sim 3.39$, 5.04, 3.33, and 3.37; and $\chi^2(\%) \sim 2.08$, 2.07, 2.20, and 1.50, respectively, for $Fd\bar{3}m$, $F\bar{4}3m$, $R\bar{3}m$, and $R3m$. Out of these structures, the $R3m$ space group is a polar structure and fits the best. The comparison of the refinements at 90 K with both the high-T $Fd\bar{3}m$ and the proposed $R3m$ space group is shown in Fig. 6(c). A satisfactory refinement of the diffraction pattern using $R3m$ space group at 90 K is depicted by the solid curve in Fig. 6(d), where the inset shows the satisfactory refinement in a selected 2θ region. The refined coordinates are Zn1 (0, 0, 0.375), Zn2 (0, 0, 0.675), Fe1 (0, 0, 0), Fe2 [0.8333(4), 0.1666(7), 0.1666(7)], O1 [0, 0, 0.2257(9)], O2 [0.1641(8), 0.8357(6), 0.0566(1)], O3 [0, 0, 0.7525(3)], and O4 [0.502(0), 0.497(0), 0.2339(0)] at 90 K.

Thermal variations of the lattice constants, as obtained from the refinement, are depicted in Fig. 6(e). With decreasing T, the lattice constant (a), crystallized in $Fd\bar{3}m$, decreases almost systematically down to T_{FE1}. A structural transition to a polar $R3m$ space group is proposed at T_{FE1}, as depicted in the figure. The lattice constants c and a close to T_N and T_{FE2} are highlighted with T in Figs. 6(f) and 6(g), respectively. As shown in Fig. 6(g), the a exhibits a discontinuous fall at T_{FE2}. The $c(T)$ in Fig. 6(f) exhibits a broadened maximum in $a(T)$ close to T_{FE2}. The unit-cell volume (V) is shown in Fig. 6(h), which exhibits a steplike change at T_{FE1}, pointing to a first-order phase transition. We note that the contraction

of V below T_{FE1} is remarkable as $\sim 0.04\%$. The T-variation at low-T is further highlighted in Fig. 6(i). The weak signature of T_N may be noted in $V(T)$, pointing to a magnetoelastic coupling. However, a definite signature in $V(T)$ is observed at T_{FE2}, below which the unit-cell volume contracts sharply. The result proposes that further structural distortion in the polar $R3m$ structure correlates with the occurrence of another FE transition at low-T.

The FE order in AFe_2O_4-type ferrite has been reported for Fe_3O_4 [66,67] and $NiFe_2O_4$ [8]. The origin of the FE order in ZFO is different from the recently observed ferroelectricity in $NiFe_2O_4$ as well as Fe_3O_4, having inverse spinel structure at room temperature [8]. Here, T_{FE1} is observed at much higher than T_N, whereas the T_{FE1} in $NiFe_2O_4$ and Fe_3O_4 was reported much below T_N and found to correlate with the structural distortions. Here, the appearance of the FE order at $T_{FE1} = 110$ K is a rare consequence, because the FE order is associated with a short-range magnetic order, which is much above T_N (~ 8 times T_N). Current results are analogous to the proposed short-range order driven occurrence of the FE order from the recent calculations [68]. In fact, the FE order coexisting with the SRO has been reported in a few occasions, such as spinel chromate [13], and a few spin-chain compounds [45,69]. Additionally, we note that the ME coupling is considerably below T_{FE1}. This has also been observed for the spin-chain compounds exhibiting FE order, which was associated with SRO [45,69]. The increase in P-value in ZFO may be correlated with the additional structural distortion in multiferroic $CoCr_2S_4$, driven by the magnetic field [14]. We further note that the P-value below T_N for ZFO does not change convincingly with the magnetic field when a separate polarization measurement is carried out close to T_N, as evident in Fig. 5(d). The result infers that neither the long-range-ordered state nor the structural distortion, giving rise to the additional electric polarization below T_N, is influenced by the magnetic field. Thus, the more plausible reason for the change in P-value in the high-T region due to magnetic field may involve the coexistence of electric polarization with SRO, where the spins are easily polarized by the magnetic field in the SRO state. Therefore, the role of SRO needs to be explored for improving ME coupling in multiferroics.

The ZFO experiences a large magnetic frustration, as indicated by the large Θ/T_N ratio [26], which is attributed to the pyrochlore structure formed by the Fe atoms in the spinel structure. Recently, the release of geometric magnetic frustration has been proposed by a strong isostructural transition in the extensively investigated $CaBaCo_4O_7$ [70], which was found to be associated with the occurrence of FE order [71–74]. Here, we observe a structural transition to a polar $R3m$ structure from the cubic spinel structure, at which a FE order appears, coexisting with the SRO in ZFO. The result may suggest that the release of the geometric magnetic frustration due to the antiferromagnetically exchange-coupled pyrochlore structure correlates with the strong structural transition. We further note that the structural change at T_{FE1} in ZFO is quite analogous to the most studied multiferroic $BiFeO_3$, where the $R3m$ structure provides a rhombohedral distortion of the pseudocubic high-T perovskite structure formed by the Bi atoms. This structural distortion correlates with emergence of the FE order [37,38].
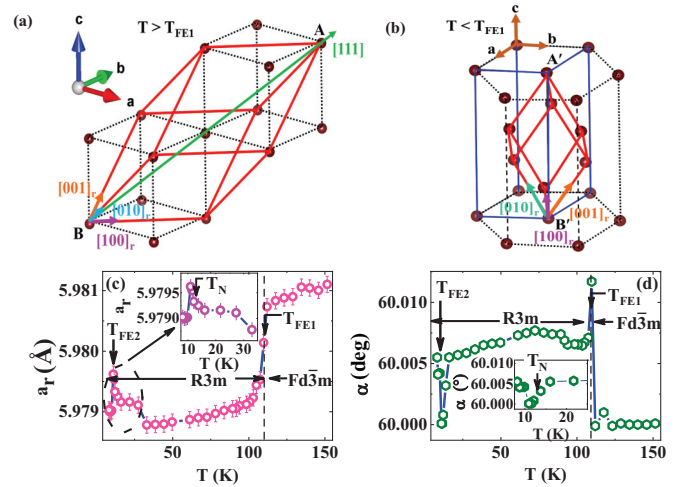

FIG. 7. (a) Connecting cubic unit cell along the [111] direction formed by Fe1 (0,0,0) atoms at the corner of the unit cell of $Fd\bar{3}m$ structure and a rhombohedral structure shown by the thick red colored lines. Axes of the rhombohedral structure are defined as $[100]_r$, $[010]_r$, and $[001]_r$. (b) Hexagonal structure formed by Fe1 (0,0,0) atoms crystallized in $R3m$ space group and formation of a rhombohedral structure. The T variations of (c) lattice constants, a_r, and (d) α of the isohedral rhombohedron, showing T_{FE1}, T_{FE2}, and T_N by the arrows.

Here, the structural transition to the $R3m$ space group from the cubic spinel structure also involves the strong rhombohedral distortions, as produced by the Fe atoms in ZFO. The results of the rhombohedral distortion, for example led by the Fe1 atoms, are summarized in Fig. 7. Here, the single Fe (0,0,0) site in the $Fd\bar{3}m$ structure divides into two Fe sites (Fe1 and Fe2) in the $R3m$ structure. We note that the Fe2 atoms also produce similar distortion. Figure 7(a) depicts the relation between the cubic structures connected along the [111] direction, as indicated by the green arrow, which are formed by the Fe1 (0,0,0) atoms in the $Fd\bar{3}m$ structure, and a pseudorhombohedral structure, as indicated by the thick red lines. These atomic arrangements are analogous to the atomic arrangements of Bi (0,0,0) in the cubic perovskite structure of $BiFeO_3$ [37]. In the figure, the three arrows located at B are the axes of the rhombohedral structure, which are described as $[100]_r$, $[010]_r$, and $[001]_r$. Here, AB is defined as $d_{[111]}$, which is the diagonal distance along the [111] direction of the rhombohedral structure. Below the structural transition, the possible rhombohedral structure formed by the Fe1 (0,0,0) atoms, crystallized in the $R3m$ space group, is defined by the thick red lines, as depicted in Fig. 7(b). Similar to that defined in Fig. 7(a), the arrows at B' are the axes of the rhombohedral structure. In the $R3m$ structure, the c axis direction exactly matches with the [111] direction of the isohedral rhombohedron, which is defined along the $B'A'$ direction in Fig. 7(b).

Thermal variations of the rhombohedral lattice constant, a_r, and the angle (α) of the isohedral rhombohedron are depicted in Figs. 7(c) and 7(d), respectively. The steplike decrease in $a_r(T)$, which is significant as $\sim 0.02\%$, is observed close to T_{FE1}. Here, the $a_r(T)$ is considered as half of AB in Fig. 7(a), having high-T $Fd\bar{3}m$ structure. Below T_{FE1}, the $a_r(T)$ decreases systematically until ~ 30 K, below which an

anomalous increase in $a_r(T)$ is observed, as highlighted in the inset of Fig. 7(c). Below T_N it shows a sharp peak, around which T_{FE2} is observed, as indicated by an arrow in Fig. 7(c). As depicted in Fig. 7(d), $\alpha(T)$ is nearly T-independent above the structural transition, and a steplike rise in α is observed from $60°$ to $60.011°$. Below T_{FE1}, $\alpha(T)$ shows a broadened maximum around ~ 70 K, following a slow decrease. A sharp "dip" in $\alpha(T)$ is observed at T_{FE2}, as indicated by an arrow in Fig. 7(d), around which a sharp peak in $a_r(T)$ is also noted. Therefore, another rhombohedral distortion at T_{FE2} correlates the low-T FE order. The possible glassy magnetic state and/or AFM order might also be involved with the occurrence of low-T FE order. We note that the geometric magnetic frustration driven by the pyrochlore structure formed by the Fe atoms in $ZnFe_2O_4$ plays a significant role, which correlates with the glassy magnetic behavior and the occurrence of AFM order at reduced temperature. Thus, the structural distortion, glassy magnetic state, and AFM order correlate with the observed low-T FE order, which needs to be explored in further studies.

IV. SUMMARY AND CONCLUSION

In summary, the experimental observations are focused mainly on two issues: (i) the high-T results close to T_{FE1} and (ii) the low-T results below T_N. The high-T results are focused on the structural transition to a polar $R3m$ space group from the cubic spinel structure close to ~ 110 K. The strong rhombohedral distortion at the structural transition leads to the emergence of the spontaneous electric polarization, which is associated with a short-range magnetic order. A considerable ME coupling, as indicated by a $\sim 7.2\%$ increase in polarization due to a 5 T magnetic field at the liquid nitrogen temperature, is noted below T_{FE1}. Intriguingly, the FE polarization is further increased below T_N, which links to another anomalous rhombohedral distortion.

The low-T magnetization results reveal the intricate magnetic phase separation between a glassy magnetic component and an AFM component, proposing a reentrant spin-glass-like state. The magnetic memory effect proposes the glassy magnetic component below T_N. The pinning mechanism at the interface between these two magnetic components driven by the magnetic field-cooling leads to the EB effect below T_N. $ZnFe_2O_4$ attracts the attention of the community due to the rare occurrence of multiferroic order, which correlates closely with the strong rhombohedral distortion, analogous to that observed in $BiFeO_3$.

[1] P. G. Radaelli, Y. Horibe, M. J. Gutmann, H. Ishibashi, C. H. Chen, R. M. Ibberson, Y. Koyama, Y.-S. Hor, V. Kiryukhin, and S.-W. Cheong, Nature (London) **416**, 155 (2002).

[2] A. Krimmel, M. Mücksch, V. Tsurkan, M. M. Koza, H. Mutka, and A. Loidl, Phys. Rev. Lett. **94**, 237402 (2005).

[3] V. Fritsch, J. Hemberger, N. Büttgen, E.-W. Scheidt, H.-A. Krug von Nidda, A. Loidl, and V. Tsurkan, Phys. Rev. Lett. **92**, 116401 (2004).

[4] A. Krimmel, V. Tsurkana, D. Sheptyakov, and A. Loidl, Physica B **378-380**, 583 (2006).

[5] S. Giri, H. Nakamura, and T. Kohara, Phys. Rev. B **72**, 132404 (2005).

[6] P. T. Barton, M. C. Kemei, M. W. Gaultois, S. L. Moffitt, L. E. Darago, R. Seshadri, M. R. Suchomel, and B. C. Melot, Phys. Rev. B **90**, 064105 (2014).

[7] A. Chatterjee, J. K. Dey, S. Majumdar, A.-C. Dippel, O. Gutowski, M. v. Zimmermann, and S. Giri, Phys. Rev. Mater. **3**, 104403 (2019).

[8] J. K. Dey, A. Chatterjee, S. Majumdar, A.-C. Dippel, O. Gutowski, M. v. Zimmermann, and S. Giri, Phys. Rev. B **99**, 144412 (2019).

[9] K. Tomiyasu, J. Fukunaga, and H. Suzuki, Phys. Rev. B **70**, 214434 (2004).

[10] Y. Amiel, G. Kh. Rozenberg, N. Nissim, A. Milner, M. P. Pasternak, M. Hanfland, and R. D. Taylor, Phys. Rev. B **84**, 224114 (2011).

[11] Y. Yamasaki, S. Miyasaka, Y. Kaneko, J.-P. He, T. Arima, and Y. Tokura, Phys. Rev. Lett. **96**, 207204 (2006).

[12] Q. Zhang, K. Singh, F. Guillou, C. Simon, Y. Breard, V. Caignaert, and V. Hardy, Phys. Rev. B **85**, 054405 (2012).

[13] K. Dey, S. Majumdar, and S. Giri, Phys. Rev. B **90**, 184424 (2014).

[14] K. Dey, A. Karmakar, A. Indra, S. Majumdar, U. Rütt, O. Gutowski, M. v. Zimmermann, and S. Giri, Phys. Rev. B **92**, 024401 (2015).

[15] S.-H. Lee, H. Takagi, D. Louca, M. Matsuda, S. Ji, H. Ueda, Y. Ueda, T. Katsufuji, J.-H. Chung, S. Park, S.-W. Cheong, and C. Broholm, J. Phys. Soc. Jpn. **79**, 011004 (2010).

[16] A. P. Ramirez, Annu. Rev. Mater. Sci. **24**, 453 (1994).

[17] J. S. Gardner, M. J. P. Gingras, and J. E. Greedan, Rev. Mod. Phys. **82**, 53 (2010).

[18] S. T. Bramwell and M. J. P. Gingras, Science **294**, 1495 (2001).

[19] S. T. Bramwell, M. J. Harris, B. C. den Hertog, M. J. P. Gingras, J. S. Gardner, D. F. McMorrow, A. R. Wildes, A. Cornelius, J. D. M. Champion, R. G. Melko, and T. Fennell, Phys. Rev. Lett. **87**, 047205 (2001).

[20] K. Matsuno, T. Katsufuji, S. Mori, Y. Moritomo, A. Machida, E. Nishibori, M. Takata, M. Sakata, N. Yamamoto, and H. Takagi, J. Phys. Soc. Jpn. **70**, 1456 (2001).

[21] K. Matsuno, T. Katsufuji, S. Mori, M. Nohara, A. Machida, Y. Moritomo, K. Kato, E. Nishibori, M. Takata, M. Sakata, K. Kitazawa, and H. Takagi, Phys. Rev. Lett. **90**, 096404 (2003).

[22] G. B. Sim and S. B. Lee, Phys. Rev. B **98**, 014423 (2018).

[23] Y. V. Tymoshenko, Y. A. Onykiienko, T. Múller, R. Thomale, S. Rachel, A. S. Cameron, P. Y. Portnichenko, D. V. Efremov, V. Tsurkan, D. L. Abernathy, J. Ollivier, A. Schneidewind, A.

Piovano, V. Felea, A. Loidl, and D. S. Inosov, Phys. Rev. X **7**, 041049 (2017).

[24] J. M. Hastings and L. M. Corliss, Rev. Mod. Phys. **25**, 114 (1953).

[25] W. Schiessl, W. Potzel, H. Karzel, M. Steiner, G. M. Kalvius, A. Martin, M. K. Krause, I. Halevy, J. Gal, W. Schäfer, G. Will, M. Hillberg, and R. Wäppling, Phys. Rev. B **53**, 9143 (1996).

[26] K. Kamazawa, Y. Tsunoda, H. Kadowaki, and K. Kohn, Phys. Rev. B **68**, 024412 (2003).

[27] D. J. Singh, M. Gupta, and R. Gupta, Phys. Rev. B **63**, 205102 (2001).

[28] C. Cheng, Phys. Rev. B **78**, 132403 (2008).

[29] M. Gaudon, N. Pailhé, A. Wattiaux, and A. Demourgues, Mater. Res. Bull. **44**, 479 (2009).

[30] J. Melo Quintero, K. L. Salcedo Rodríguez, G. A. Pasquevich, P. Mendoza Zélis, S. J. Stewart, C. E. Rodríguez Torres, and L. A. Errico, Hyperfine Interact. **237**, 63 (2016).

[31] E. Greenberg, W. M. Xu, M. Nikolaevsky, E. Bykova, G. Garbarino, K. Glazyrin, D. G. Merkel, L. Dubrovinsky, M. P. Pasternak, and G. Kh. Rozenberg, Phys. Rev. B **95**, 195150 (2017).

[32] K. L. Salcedo Rodríguez, S. J. Stewart, P. M. Mendoza Zélis, G. A. Pasquevich, and C. E. Rodríguez Torres, J. Alloys Compd. **752**, 289 (2018).

[33] J. J. Melo Quintero, C. E. Rodríguez Torres, and L. A. Errico, J. Alloys Compd. **741**, 746e755 (2018).

[34] K. Kamazawa, Y. Tsunoda, K. Odaka, and K. Kohn, J. Phys. Chem. Solids **60**, 1261 (1999).

[35] K. Kamazawa, S. Katano, and Y. Tsunoda, Physica B **345**, 96 (2004).

[36] Y. Fei, S. J. Kennedy, S. J. Campbell, and M. Hofmann, Physica B **356**, 264 (2005).

[37] F. Kubel and H. Schmid, Acta Crystallogr. **B46**, 698 (1990).

[38] J.-G. Park, M. D. Le, J. Jeong, and S. Lee, J. Phys.: Condens. Matter **26**, 433202 (2014).

[39] Y. Hou, X. Li, Q. Zhaoa, and G. Chen, Appl. Catal. B **142**, 80 (2013).

[40] M. Wang, Z. Ai, and L. Zhang, J. Phys. Chem. C **112**, 13163 (2008).

[41] H. Song, L. Zhu, Y. Li, Z. Lou, M. Xiao, and Z. Ye, J. Mater. Chem. A **3**, 8353 (2015).

[42] M. I. Mendelson, J. Am. Ceram. Soc. **52**, 443 (1969).

[43] J. A. Mydosh, *Spin Glasses: An Experimental Introduction* (Taylor & Francis, London, 1993).

[44] Y. Sun, M. B. Salamon, K. Garnier, and R. S. Averback, Phys. Rev. Lett. **91**, 167206 (2003).

[45] A. Indra, K. Dey, S. Majumdar, I. Sarkar, S. Francoual, R. P. Giri, N. Khan, P. Mandal, and S. Giri, Phys. Rev. B **95**, 094402 (2017).

[46] D. De, A. Karmakar, M. K. Bhunia, A. Bhaumik, S. Majumdar, and S. Giri, J. Appl. Phys. **111**, 033919 (2012).

[47] J. K. Dey, S. Majumdar, and S. Giri, J. Phys.: Condens. Matter **30**, 235801 (2018).

[48] S. Giri, M. Patra, and S. Majumdar, J. Phys.: Condens. Matter **23**, 073201 (2011).

[49] W. H. Meiklejohn and C. P. Bean, Phys. Rev. **102**, 1413 (1956).

[50] W. H. Meiklejohn and C. P. Bean, Phys. Rev. **105**, 904 (1957).

[51] J. Nogues and I. K. Schuller, J. Magn. Magn. Mater. **192**, 203e232 (1999).

[52] P. J. van der Zaag, A. R. Ball, L. F. Feiner, and R. M. Wolf, J. Appl. Phys. **79**, 5103 (1996).

[53] P. J. van der Zaag, R. M. Wolf, A. R. Ball, C. Bordel, L. F. Feiner, and R. Jungblut, J. Magn. Magn. Mater. **148**, 346 (1995).

[54] S. Sabyasachi, M. Patra, S. Majumdar, S. Giri, S. Das, V. S. Amaral, O. Iglesias, W. Borghols, and T. Chatterji, Phys. Rev. B **86**, 104416 (2012).

[55] M. Thakur, M. Patra, K. De, S. Majumdar, and S. Giri, J. Phys.: Condens. Matter **20**, 195215 (2008).

[56] K. De, M. Patra, S. Majumdar, and S. Giri, J. Phys. D **41**, 175007 (2008).

[57] P. M. Shand, T. Rash, M. Streicher, T. E. Kidd, K. R. Boyle, and L. H. Strauss, Phys. Rev. B **82**, 214413 (2010).

[58] T. N. M. Ngo, U. Adem, and T. T. M. Palstra, Appl. Phys. Lett. **106**, 152904 (2015).

[59] N. Terada, Y. S. Glazkova, and A. A. Belik, Phys. Rev. B **93**, 155127 (2016).

[60] R. Chen and Y. Kirsh, *Analysis of Thermally Stimulated Process* (Pergamon, New York, 1981).

[61] T. D. Sparks, M. C. Kemei, P. T. Barton, R. Seshadri, E.-D. Mun, and V. S. Zapf, Phys. Rev. B **89**, 024405 (2014).

[62] N. Mufti, A. A. Nugroho, G. R. Blake, and T. T. M. Palstra, J. Phys.: Condens. Matter **22**, 075902 (2010).

[63] T. Kimura, S. Kawamoto, I. Yamada, M. Azuma, M. Takano, and Y. Tokura, Phys. Rev. B **67**, 180401(R) (2003).

[64] A. Indra, K. Dey, J. K. Dey, S. Majumdar, U. Rütt, O. Gutowski, M. v. Zimmermann, and S. Giri, Phys. Rev. B **98**, 014408 (2018).

[65] B. J. Campbell, H. T. Stokes, D. E. Tanner, and D. M. Hatch, J. Appl. Crystallogr. **39**, 607 (2006).

[66] K. Kato and S. Iida, J. Phys. Soc. Jpn. **51**, 1335 (1982).

[67] Y. Miyamoto, M. Kobayashi, and S. Chikazumi, J. Phys. Soc. Jpn. **55**, 660 (1986).

[68] X. Wan, H.-C. Ding, S. Y. Savrasov, and C.-G. Duan, Sci. Rep. **6**, 22743 (2016).

[69] T. Basu, V. V. Ravi Kishore, S. Gohil, K. Singh, N. Mohapatra, S. Bhattacharjee, B. Gonde, N. P. Lalla, P. Mahadevan, S. Ghosh, and E. V. Sampathkumaran, Sci. Rep. **4**, 5636 (2014).

[70] V. Caignaert, V. Pralong, V. Hardy, C. Ritter, and B. Raveau, Phys. Rev. B **81**, 094417 (2010).

[71] V. Caignaert, A. Maignan, K. Singh, Ch. Simon, V. Pralong, B. Raveau, J. F. Mitchell, H. Zheng, A. Huq, and L. C. Chapon, Phys. Rev. B **88**, 174403 (2013).

[72] R. S. Fishman, S. Bordács, V. Kocsis, I. Kézsmárki, J. Viirok, U. Nagel, T. Röm, A. Puri, U. Zeitler, Y. Tokunaga, Y. Taguchi, and Y. Tokura, Phys. Rev. B **95**, 024423 (2017).

[73] K. Dey, A. Indra, A. Chatterjee, S. Majumdar, U. Rütt, O. Gutowski, M. v. Zimmermann, and S. Giri, Phys. Rev. B **96**, 184428 (2017).

[74] C. Dhanasekhar, A. K. Das, Ripandeep Singh, A. Das, G. Giovannetti, D. Khomskii, and A. Venimadhav, Phys. Rev. B **96**, 134413 (2017).